Ocean Engineering 150 (2018) 298–308

Contents lists available at ScienceDirect

Ocean Engineering

journal homepage: www.elsevier.com/locate/oceaneng

A numerical and experimental study of internal solitary wave loads on semi-submersible platforms

Xu Wang [a,*], Ji-Fu Zhou [a,b,**], Zhan Wang [a,b], Yun-Xiang You [c]

[a] Key Laboratory for Mechanics in Fluid Solid Coupling System, Institute of Mechanics, Chinese Academy of Sciences, Beijing 100190, China
[b] School of Engineering Sciences, University of Chinese Academy of Sciences, Beijing 100049, China
[c] State Key Laboratory of Ocean Engineering, Shanghai Jiao Tong University, Shanghai 200240, China

ARTICLE INFO

Keywords:
Internal solitary waves
Semi-submersible platform
Wave loads

ABSTRACT

Using a double-plate wave maker, a series of laboratory experiments of internal solitary wave (ISW) loads on semi-submersible platforms were conducted in a density stratified fluid tank. Combined with experimental results, a numerical flume based on the Navier-Stokes equations in a two-layer fluid is developed to simulate nonlinear interactions between ISWs and a semi-submersible platform. The numerical results of horizontal and vertical forces, as well as torques on the semi-submersible platform also agree well with the experimental measurements. Besides, the numerical results indicate that the horizontal and vertical forces on the semi-submersible platform due to ISWs can be divided into three components, namely the wave pressure-difference forces, viscous pressure-difference forces, and the frictional force which is negligible. For the horizontal force, the wave and viscous pressure-difference components are of the same order, implying that the viscous effect is significant. For the vertical force, the contribution of the viscous pressure-difference is not important. Moreover, the diffraction effect is significant for horizontal force and insignificant for vertical force. Hence, it is feasible to estimate the vertical load using the Froude-Krylov approach.

1. Introduction

A large number of observations show that internal solitary waves (ISWs) occur frequently and exist widely in the ocean due to density stratification arising from salinity and temperature variations (Apel et al., 1985), which present significant hazards in coastal and oceanic regions where offshore petroleum exploration, production and sub-sea storage activities are in progress. (Osborne and Burch, 1980). For instance, in 1990 a sudden strong current accompanied by an internal wave caused a cable breakage in the extended test period of the Liuhua oilfield in the South China Sea (Bole et al., 1994). Therefore, drilling rigs should be built to withstand ISW loads in the areas where internal solitons may occur (Ablowitz and Clarkson, 1991).

A semi-submersible floating structure can serve as a drilling platform or an offshore wind turbine foundation. There is a large number of experimental and numerical investigations on the performance of this type of platform under the action of wind, waves and currents, and methods and software have been developed to calculate the hydrodynamic loads (Faltinsen, 1993; Kvittem et al., 2012). Nonetheless, there are relatively fewer studies on the loading mechanism of ISWs on floating structures. In general, previous researches were mainly focused on cylinder structures and adopted the Morison formula (Morison et al., 1950) to calculate ISW loads (Cai et al., 2003, 2008, 2006; Si et al., 2012; Song et al., 2011). However, the geometry of the semi-submersible platform is much more complicated than a cylinder thus it is difficult to directly calculate the ISW load by the Morison formula. Apparently, by modifying its coefficients, the Morison formula can still be used to estimate the loads on the cylindrical components of platforms, such as columns, horizontal and diagonal braces. For instance, Huang et al. (2013) and Chen et al. (2017) developed two sets of modified coefficients of the Morison formula by fitting the experimental data. However, these modified coefficients are not universal and certainly depend on the model settings. It is therefore questionable to extend the modified coefficients to other circumstances. Owing to the practical significance of the problem and the aforementioned discussion, a lot of ISW hydrodynamic issues on floating platforms should be clarified, including the mechanism of various load components, the influence of viscosity, and so on.

With the enhancement of computing capability, CFD simulations

* Corresponding author.
** Corresponding author. Key Laboratory for Mechanics in Fluid Solid Coupling System, Institute of Mechanics, Chinese Academy of Sciences, Beijing 100190, China.
E-mail address: wangxu@imech.ac.cn (X. Wang).

https://doi.org/10.1016/j.oceaneng.2017.12.042
Received 6 September 2017; Received in revised form 14 November 2017; Accepted 17 December 2017

provide an effective way to analyze the problem mentioned above. As a first step towards a comprehensive understanding, one of the key issues is to develop an accurate and controllable numerical flume for the interaction between ISWs and structures. Previously Wang et al. (2017) proposed a new method to generate ISWs by adding a mass source/sink term to the continuity equation, which has been proved effective and accurate. However, special attentions should be paid to such issues as whether the numerical waveform can match the desired one in the presence of platforms, the reliability of simulated ISW loads, and so on. In the present paper, based on wave generation method proposed and with the aid of laboratory experiments, we will develop a numerical flume to calculate ISW loads on semi-submersible platforms. Furthermore, the components of the ISW loads accounting for wave pressure, fluid viscosity and wave diffraction as well will be discussed.

The present paper is organized as follows. Section 2 briefly describes the developed numerical flume. Section 3 introduces the experimental facility and procedure. Section 4 presents the numerical results, including wave properties and the ISW load characteristics on the semi-submersible platform. Finally, conclusions are given in Section 5.

2. Numerical methods

The present numerical experiments use the full Navier-Stokes equations to simulate the nonlinear interactions between ISWs and a semi-submersible platform. The ISWs are obtained by adding a mass source/sink term to the continuity equation.

2.1. Governing equations

For an incompressible fluid of density ρ_i, the velocity components (u_i, v_i, w_i) in Cartesian coordinates $Oxyz$ (its origin is at the interface, see Fig. 1) and the pressure P_i satisfy the continuity equation and the Navier-Stokes equations:

$$u_{ix} + v_{iy} + w_{iz} = 0, \tag{1}$$

$$u_{it} + u_i u_{ix} + v_i u_{iy} + w_i u_{iz} = -p_{ix}/\rho_i + \nu\left(u_{ixx} + u_{iyy} + u_{izz}\right), \tag{2}$$

$$v_{it} + u_i v_{ix} + v_i v_{iy} + w_i v_{iz} = -p_{iy}/\rho_i + \nu\left(v_{ixx} + v_{iyy} + v_{izz}\right), \tag{3}$$

$$w_{it} + u_i w_{ix} + v_i w_{iy} + w_i w_{iz} = -p_{iz}/\rho_i + \nu\left(w_{ixx} + w_{iyy} + w_{izz}\right) - g, \tag{4}$$

where g is the gravitational acceleration, the subscripts with respect to space and time represent partial differentiation, and $i = 1$ (i=2) denotes the upper (lower) layer fluid.

In order to generate ISWs by using the mass source method, Eq. (1) is modified as

$$u_{ix} + v_{iy} + w_{iz} = \begin{cases} 0, & (x, y, z) \notin \Omega \\ S_i(x, y, z, t)/\rho_i, & (x, y, z) \in \Omega \end{cases}, \tag{5}$$

where the additional mass source term $S_i(x, y, z, t)$ is a nonzero function only in the source region Ω.

The computational domain is shown in Fig. 1, which consists of three regions: the mass source region, wave propagation region and dissipation region. Demarcated by ISW interface, the source region can be divided into two subregions Ω_1 and Ω_2, which respectively denote the source region and the sink region. Fluxes between the source and the sink are forced to cancel each other in order to ensure the conservation of mass in the computational domain.

For simplicity, we assume that the mass source functions vary with time only (namely, S_i is independent of spatial variables). We consider the interface fluctuation in the mass source region during the wave generation process, and define $S_i(t)$ as:

$$S_1(t) = -\rho_1 c \frac{\zeta(t)}{h_1 - \zeta(t)} \frac{1}{\Delta x}, \tag{6}$$

$$S_2(t) = \rho_2 c \frac{\zeta(t)}{h_2 + \zeta(t)} \frac{1}{\Delta x}, \tag{7}$$

where c denotes the phase speed, Δx is the width of the mass source region, and $\zeta(t)$ is interface displacement of an ISW (Wang et al., 2017).

2.2. Boundary and initial conditions

The rigid-lid approximation is adopted on the top in the present paper. It follows that the impermeability condition should be satisfied at the top and bottom of the fluid domain:

$$w_1|_{z=h_1} = 0, \quad w_2|_{z=-h_2} = 0. \tag{8}$$

Moreover, the surface of the platform is set to the impermeability boundary, the forces and torque on the surface are monitored during the simulation.

The normal velocity is continuous, and so is the pressure, at the interface $z = \zeta(x, y, t)$ which give the boundary conditions:

$$\zeta_t + u_1\zeta_x + v_1\zeta_y = w_1, \quad \zeta_t + u_2\zeta_x + v_2\zeta_y = w_2, \quad p_1 = p_2. \tag{9}$$

Only right-traveling ISWs are considered, so a symmetry condition is posed on the left boundary. The right boundary is specified as a smooth non-slip wall. In order to avoid wave reflection at the end, a buffering region is allocated to dissipate ISWs in the numerical flume, which is realized by adding a source term to the momentum equation in the vertical direction:

$$w_{it} + u_i w_{ix} + v_i w_{iy} + w_i w_{iz} = -p_{iz}/\rho_i + \nu\left(w_{ixx} + w_{iyy} + w_{izz}\right) - g - \delta(x)w, \tag{10}$$

where the damping function $\delta(x)$ is nonzero only in the dissipation region, otherwise $\delta(x) = 0$. In the present paper, we choose $\delta(x)$ as a linear function:

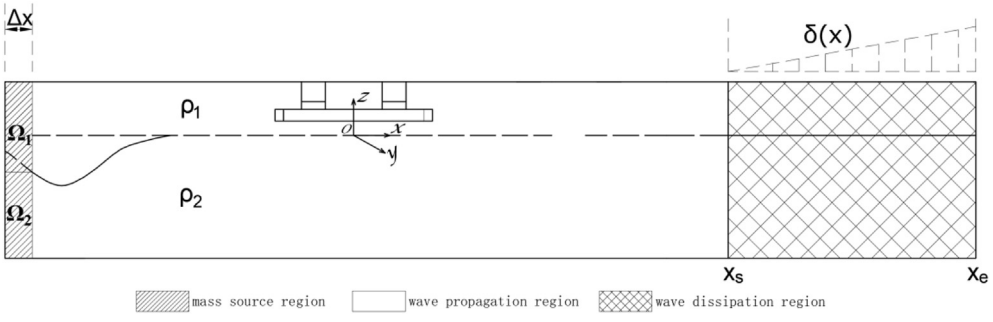

Fig. 1. The front view of the 3D computation domain.

$$\delta(x) = \alpha \frac{x - x_s}{x_e - x_s}, \tag{11}$$

where α is an empirical coefficient depending on the specific case, while x_s and x_e respectively denote the horizontal coordinates of two endpoints of the dissipation region ($x_s < x_e$).

There is no wave or current in the computation domain at the initial moment, indicating that both the velocity and velocity gradient are zero at t = 0.

2.3. Interface treatment

The VOF (volume of fluid) method (Hirt and Nichols, 1981) is employed to track the ISW interface. The VOF equation can be written as follows:

$$\frac{\partial a_i}{\partial t} + \frac{\partial}{\partial x}(a_i u) + \frac{\partial}{\partial y}(a_i v) + \frac{\partial}{\partial z}(a_i w) = \frac{s_{a_i}}{\rho_i}, \tag{12}$$

where a_i is the volume fraction for fluid i ($i = 1, 2$). For every single controlled volume, the total volume fraction is unit (i.e. $a_1 + a_2 = 1$), and each component meets one of the following situations: (1) $a_i = 0$: the cell is empty of fluid i; (2) $a_i = 1$: the cell is full of fluid i; (3) $0 < a_i < 1$: the cell contains the interface between two fluids.

2.4. Forces on a semi-submersible platform

At the experiment stage, the horizontal force F_x, vertical force F_z and torque M_y are measured by the three-component force balance. Correspondingly these loads and torque are also monitored during the simulation. Lateral force F_y (caused by periodic trailing vortex behind the semi-submersible platform) is much less than F_x or F_z, so it is not discussed in the paper. The F_x and F_z on a semi-submersible platform can be expressed as:

$$F_x = \mu \int_s \left(\left(\frac{\partial u}{\partial y} + \frac{\partial v}{\partial x} \right) n_y + \left(\frac{\partial u}{\partial z} + \frac{\partial w}{\partial x} \right) n_z \right) ds + \int_s -p n_x ds, \tag{13}$$

$$F_z = \mu \int_s \left(\left(\frac{\partial u}{\partial z} + \frac{\partial w}{\partial x} \right) n_x + \left(\frac{\partial v}{\partial z} + \frac{\partial w}{\partial y} \right) n_y \right) ds + \int_s -p n_z ds, \tag{14}$$

where μ denotes the dynamic viscosity of water ($1.01 \times 10^{-3}\ N \cdot \frac{s}{m^2}$), S is the wetted surface of the semi-submersible platform, and $(n_x,\ n_y,\ n_z)$ is the outward unit normal vector of the surface. In the formulas, the forces consist of two parts, where the first term represents the friction (f_x, f_z) and the second one represents the pressure-difference force (F_x^p, F_z^p).

$$F_x^p = \int_s -p n_x ds, \tag{15}$$

$$F_z^p = \int_z -p n_z ds, \tag{16}$$

$$f_x = \mu \int_s \left(\left(\frac{\partial u}{\partial y} + \frac{\partial v}{\partial x} \right) n_y + \left(\frac{\partial u}{\partial z} + \frac{\partial w}{\partial x} \right) n_z \right) ds, \tag{17}$$

$$f_z = \mu \int_s \left(\left(\frac{\partial u}{\partial z} + \frac{\partial w}{\partial x} \right) n_x + \left(\frac{\partial v}{\partial z} + \frac{\partial w}{\partial y} \right) n_y \right) ds. \tag{18}$$

Furthermore, according to the contribution of the viscosity, the pressure-difference force can be divided into two components: wave pressure-difference force (F_x^{pw}, F_z^{pw}) and viscous pressure-difference force (F_x^{pv}, F_z^{pv}). The wave pressure-difference force is associated with the fluctuation of water parcels, which can be calculated based on the Euler equations, while the viscous pressure-difference force is associated with the viscous effect, which can be calculated by subtracting the wave pressure-difference force obtained by the Euler equations from the one obtained by the Navier-Stokes (N-S) equations. The expressions of (F_x^{pw}, F_z^{pw}) and (F_x^{pv}, F_z^{pv}) are given as:

$$F_x^{pw} = \int_s -p n_x ds\ _{(\text{Euler})}, \tag{19}$$

$$F_z^{pw} = \int_s -p n_z ds\ _{(\text{Euler})}, \tag{20}$$

$$F_x^{pv} = \int_s -p n_x ds\ _{(\text{N-S})} - \int_s -p n_x ds\ _{(\text{Euler})}, \tag{21}$$

$$F_z^{pv} = \int_s -p n_z ds\ _{(\text{N-S})} - \int_s -p n_z ds\ _{(\text{Euler})}. \tag{22}$$

To facilitate comparison with experiment measurements, the moment center is placed at the joint point of the experiment model and the three-component force balance (see Fig. 4(a)). Considering the symmetry of the model and neglecting the slightly nonuniform distribution of the vertical force over the horizontal wetted surfaces of the structure, we have the torque M_y given by

$$M_y = \mu \int_s \left(\left(\frac{\partial u}{\partial y} + \frac{\partial v}{\partial x} \right) n_y + \left(\frac{\partial u}{\partial z} + \frac{\partial w}{\partial x} \right) n_z \right) \cdot \bar{d} \cdot ds + \int_s -p n_x \cdot \bar{d} \cdot ds, \tag{23}$$

where $\bar{d}$ is the arm of the horizontal force of each wetted cell of the structure, namely the vertical distance between the cell center and the moment center.

3. Experimental facility and procedure

A series of experiments is conducted in the large-scale density stratified tank (length: 30 m, width: 0.6 m, height: 1.2 m) at Shanghai Jiao Tong University (see Fig. 2). The fluid in the tank is stratified into two

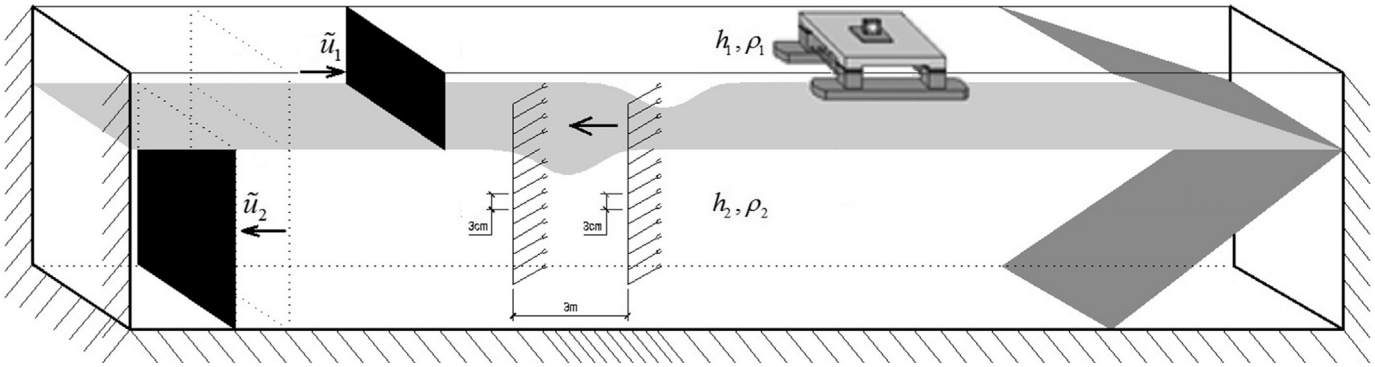

Fig. 2. Principle of internal solitary wave generated by a double-plate wave maker (identified by black).

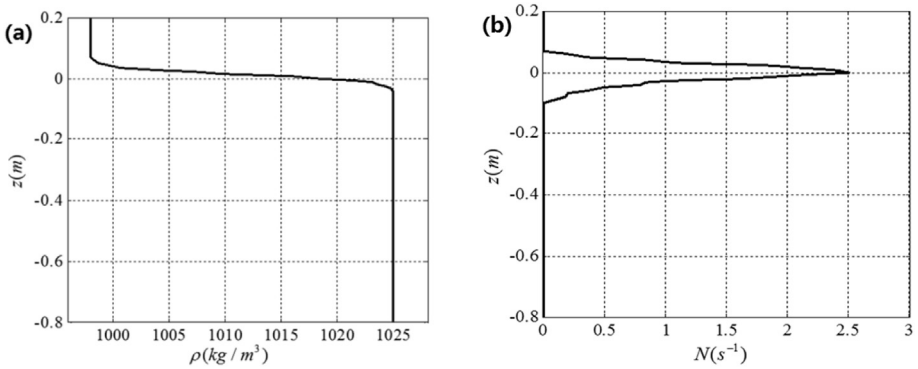

Fig. 3. The density (a) and Brunt–Väisälä frequency (b) of the stratified fluid in the tank for $h_1 : h_2 = 20 : 80$.

layers with the injection method. We first inject fresh water (density: $\rho_1 = 998kg/m^3$) till its depth equal to h_1, then slowly inject salt water (density: $\rho_2 = 1025kg/m^3$) from two mushroom-type inlets at the bottom of the tank until the total depth reaches to h, as a consequence, the salt water is of the depth $h_2 = h - h_1$. Fig. 3 shows the density and Brunt–Väisälä frequency of the stratified fluid in the tank as $h_1 : h_2 = 20 : 80$, where the Brunt–Väisälä frequency is defined as $N(z) = \sqrt{-(g/\rho_1)(\partial\rho_1/\partial z)}$.

Different from the gravity collapse method (Du et al., 2016), at the experimental stage ISWs are generated using a double-plate (identified by black) wave maker, and the procedure is similar to that described by Wessels and Hutter (1996). In order to generate nonlinear ISWs with higher amplitudes, the drive mechanism of the wave-maker is significantly upgraded and the control software of two plates is modified. Besides, a steel plate (with adjusted size through tests) is put on the top of the wave-maker to weaken the disturbance of the free surface. In addition, a wedge-shape wave breaker is set up at the end (right end in Fig. 2) of the tank to prevent solitary waves from reflecting. The two steel plates

Table 1
The numerical experiments under the action between ISWs and platforms.

Case ID	h_1/(m)	h_2/(m)	A/(m)	ISW theory	*Re*
A1	0.2	0.8	0.053	KdV	5.5e4
A2	0.2	0.8	0.106	eKdV	7.8e4
A3	0.2	0.8	0.148	eKdV	9.8e4
A4	0.2	0.8	0.172	eKdV	1.1e5
A5	0.2	0.8	0.225	MCC	2.1e5
B1	0.25	0.75	0.049	KdV	6.0e4
B2	0.25	0.75	0.097	eKdV	8.7e4
B3	0.25	0.75	0.109	eKdV	9.4e4
B4	0.25	0.75	0.135	eKdV	1.1e5
B5	0.25	0.75	0.154	eKdV	1.2e5
C1	0.3	0.7	0.0652	KdV	8.1e4
C2	0.3	0.7	0.078	eKdV	9.0e4
C3	0.3	0.7	0.094	eKdV	1.0e5
C4	0.3	0.7	0.1075	eKdV	1.1e5
C5	0.3	0.7	0.134	eKdV	1.4e5

($R_e = \frac{\lambda U_{max}}{\nu}$, where U_{max} is the maximum horizontal velocity induced by ISWs).

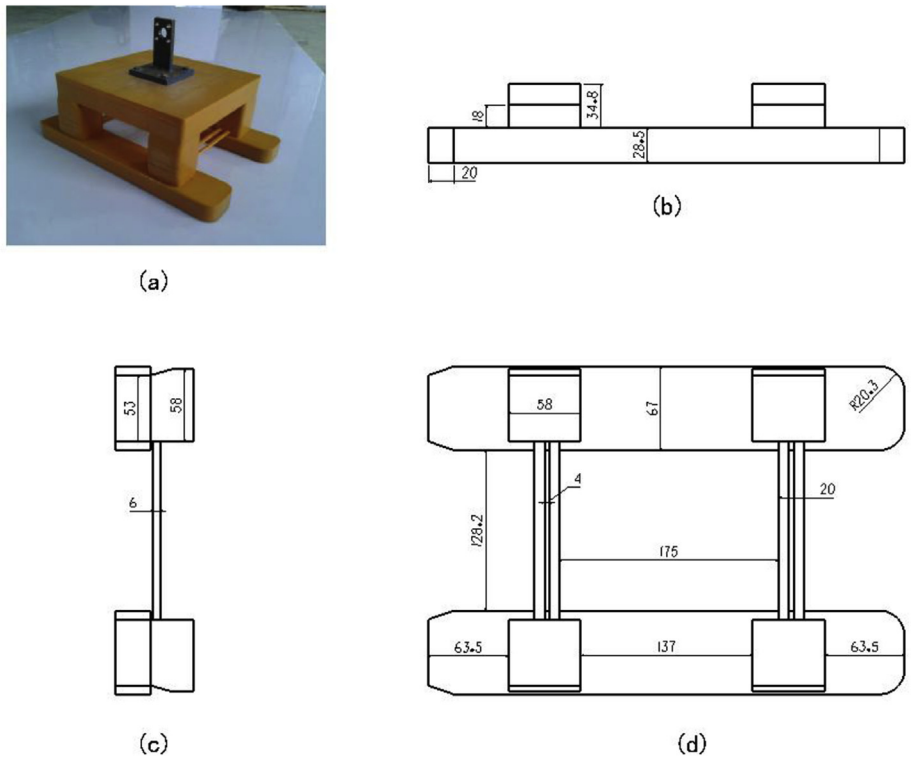

Fig. 4. (a) The experimental model; (b) the front view; (c) the right view (d) the top view (Unit: cm).

move along the opposite directions at different speeds, so as to generate an ISW at the interface between two layers. At the preparation stage, two plates are set to the same heights as undisturbed fluid layers. During the generation process, the speed of the upper and lower plates ($\overline{u}_1$, $\overline{u}_2$) are controlled by a computer and can be expressed respectively as:

$$\overline{u}_1 = -c\cdot\frac{\zeta(t)}{h_1}\Big/, \quad \overline{u}_2 = c\cdot\frac{\zeta(t)}{h_2}, \tag{24}$$

where c is the phase speed, and $\zeta(t)$ denotes the interface displacement of the desired ISW.

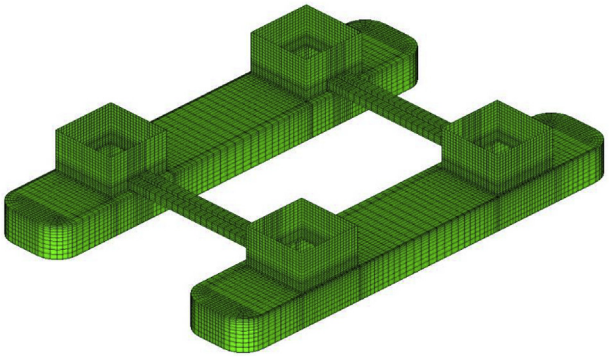

Fig. 5. The grid distribution for the wet surface of the semi-submersible platform.

ISWs are measured using two rows of conductivity probes which are arranged with 3 m apart. Each row consists of 13 equally distributed probes, and the distance between two consecutive probes is 3 cm. It is known that the conductivity has a linear relationship with density, so we can get density variations by post-processing the conductivity signal measured with the two rows of probes. As a consequence, we can easily obtain ISW interface displacement, as well as the phase speed.

In the experiment, there is always trailing-waves phenomenon behind the leading ISW. The existence of trailing waves implies the dissipation of wave energy during wave generation. Therefore, the measured amplitude is very difficult to reach the desired amplitude for a specific case. In order to generate the desired ISW waveform for a specific density stratification, firstly we have to seek the relation between the measured amplitude a_m and the desired amplitude a_d based on a series of experiments, and then the desired amplitude can be achieved by adjusting input parameters according to the relation.

The experimental model and the dimensions of the underwater part are shown in Fig. 4. The forces (F_x, F_z, M_y) on the semi-submersible platform during the ISW propagation are measured by the three-component force balance, which is connected to the model and fixed on the top of the tank. Before the experiment, an additional weight is introduced to ensure the balance between gravity and buoyancy of the model. Afterwards, we load and unload weights on the model along the horizontal and vertical directions respectively in order to obtain the calibration relationship between the measured electronic signals and loads. During the experiment, ISW loads on the model can be calculated from the electrical signals according to the calibration relationship.

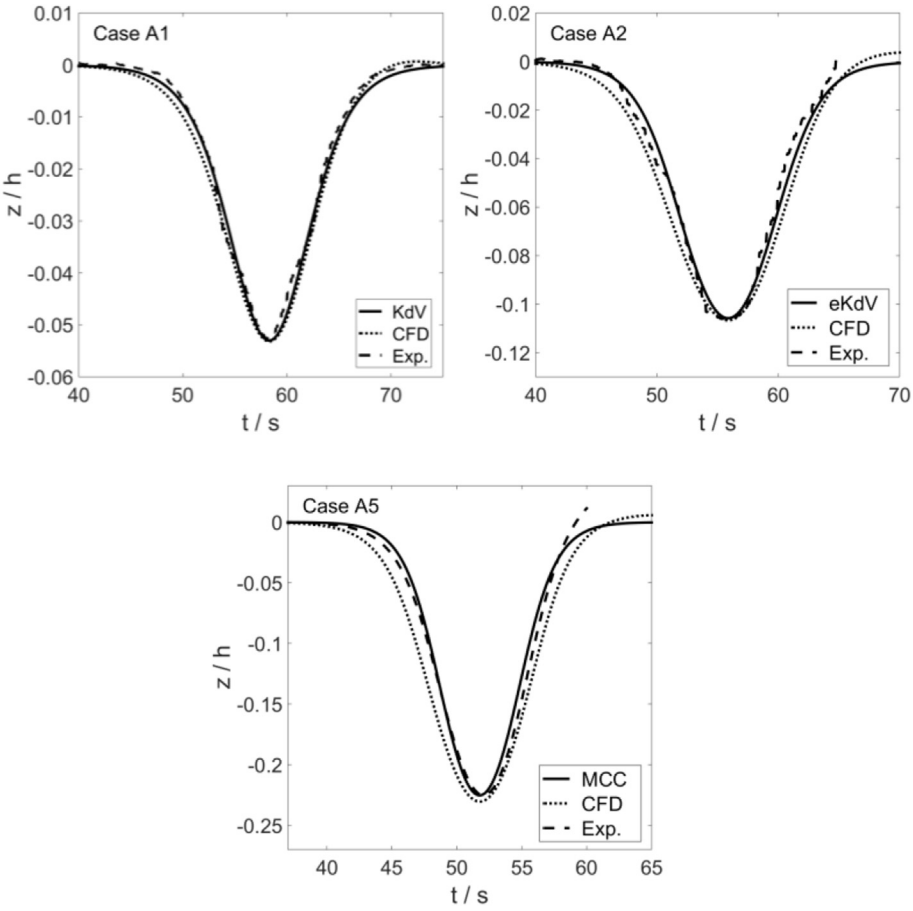

Fig. 6. Comparisons of profiles of ISWs between CFD simulations (dotted curves), theoretical models (solid curves), and laboratory experiments (dash-dotted curves) for Case A1, Case A2 and Case A5 (Note that the scales are different in the three panels).

4. Numerical results and discussions

4.1. Numerical implementation

A numerical flume is established to generate ISWs using UDF (User Defined Function) redevelopment tools on the platform of Fluent software. The numerical model works as follows: first calculate the ISW interface displacement ζ(t) by a suitable ISW theory as in Table 1, then put ζ(t) in the mass source function given by Eqs. (6) and (7), and finally the ISW is excited in the source term region. During the propagation of the ISW, the forces on the semi-submersible platform are monitored in real time.

Structured elements are used to ensure the mesh quality of the computational domain. With regard to the flume, the grids in x- and y-direction are refined to $\lambda/25$ and $\lambda/30$ respectively. The constant λ is defined as $\lambda = \frac{1}{A}\int_{x_m}^{\infty}\zeta(x)dx$ introduced by Koop and Butler (1981), where x_m is the location of the wave crest and A is the amplitude of the ISW. In z direction, the computational domain is divided into three parts: $-h_2 \le z < -A$, $-A \le z < 0$, and $0 \le z \le h_1$. Local grid refinements are employed to reduce the numerical dispersion, in the region of wave motion ($-A \le z < 0$), where the grid is refined to $A/10$. In the upper and lower regions, the grids are set to the geometric progression (common ratio is 1.03). Particularly, For the wet surface of the platform (shown in Fig. 5), the grid size need to be further refined to about $\lambda/300$.

The governing equations are discretized on three-dimension structured grids using finite volume method (FVM) and well-chosen numerical schemes are taken to avoid the spurious effects. In particular the pressure implicit with splitting of operators (PISO) algorithm is adopted to solve the pressure velocity coupling, where the spatial gradient are discretized with the Green-Gauss Node Based method together with a second-order upwind scheme for VOF volume fraction. Moreover, the temporal terms are discretized using a second-order implicit scheme, and the time step is set to 0.005s during the simulation.

Nonlinearity and dispersion are two fundamental mechanisms which govern the physics of ISWs (Camassa et al., 2006). ISWs are commonly described by the Korteweg-de Vries (KdV) equation, extended KdV (eKdV) equation, Miyata-Choi-Camassa (MCC) equation and others (Choi and Camassa, 2000; Helfrich and Melville, 2006). In the present paper, 15 numerical experiments are carried out for the interaction between ISWs and a platform under different depths and wave amplitudes (Table 1), which are in line with the experiment cases. The length of the flume is 30 m (in which $\Delta x = 0.04m$ and the width of damping region is

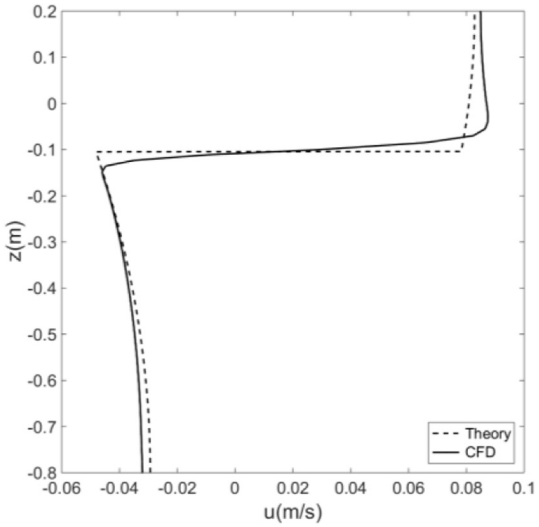

Fig. 8. The vertical profiles of horizontal velocities at the wave trough (t = 50s).

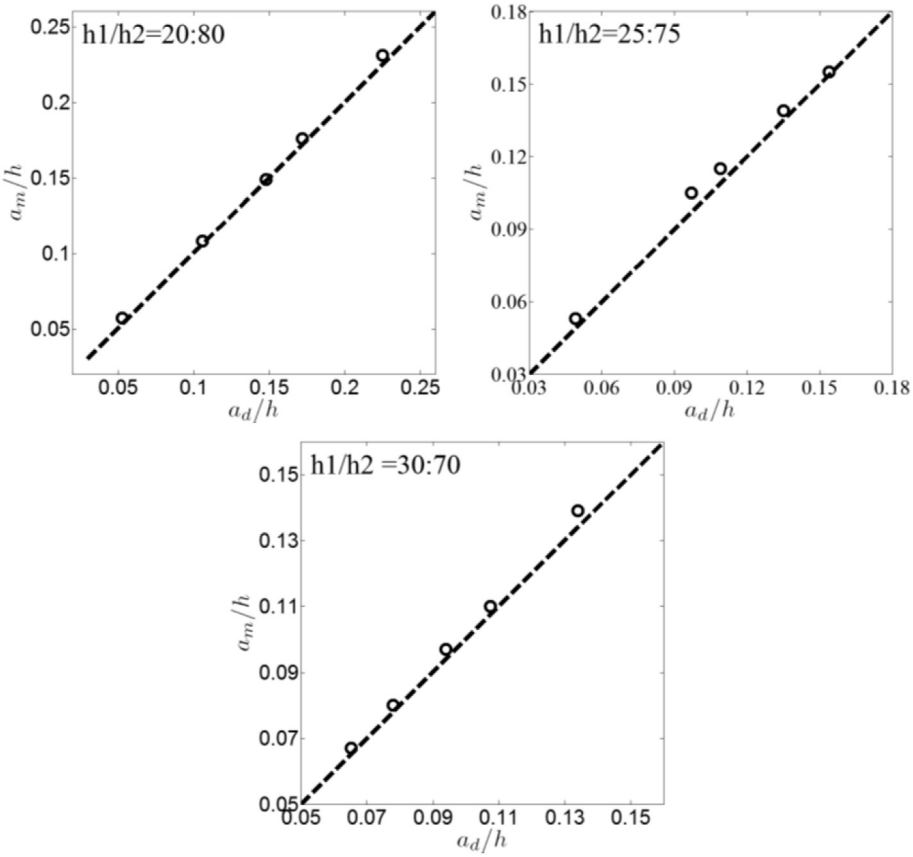

Fig. 7. The numerical results of wave amplitudes for the ISWs.

6m), the total depth is 1 m, the draft of the semi-submersible platform d is 0.633 m, the displacement volume ∇ is $1.918 \times 10^{-3}\ m^3$, the upper layer fluid density ρ_1 is 998kg/m^3, and the lower layer fluid density ρ_2 is 1025kg/m^3.

4.2. Numerical simulations for ISWs

Fig. 6 shows the comparisons for wave profiles of ISWs between CFD simulations, theories and laboratory experiments. As shown in Table 1, Case A1, Case A2 and Case A5 represent the weakly, moderately and strongly nonlinear ISWs, respectively. The wave profiles obtained by the CFD simulation are in good agreement with both the theoretical and experimental results (the relative errors are within 3%), which indicates that the numerical wave maker can accurately generate the waveform in the presence of platforms, no matter it is a weakly nonlinear ISW or a strongly nonlinear one.

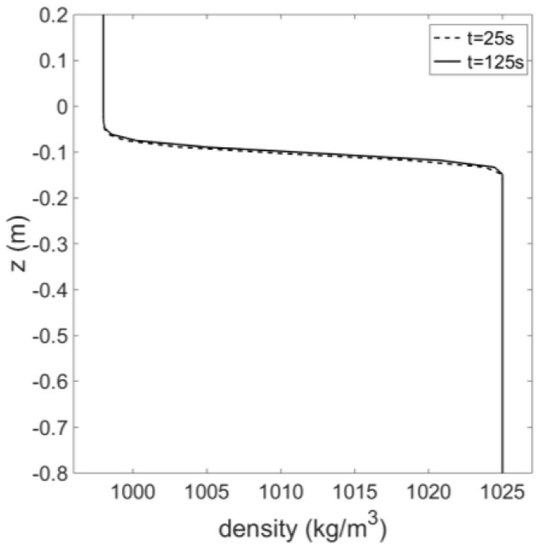

Fig. 9. The vertical profiles of density at the ISW trough (t = 25s, 125s).

The numerical results of wave amplitudes in all cases are shown in Fig. 7, where the dots represent the simulated results, and the dashed line represents the desired amplitude. It shows that the simulated amplitudes are in good agreement with the desired ones, with the maximum error less than 5%.

In order to further test the accuracy of the proposed wave generating method, the validation of velocity fields induced by ISWs in the presence of platforms is very important. Fig. 8 shows the comparisons of vertical profiles of horizontal velocities at wave troughs between the CFD simulation and theoretical prediction (t = 50s) for Case A2. In the figure, the theoretical results is based on the strongly nonlinear asymptotic approximation model in a two-fluid system proposed by Camassa et al. (2006). The Leading-order horizontal velocity can be written as:

Upper layer fluid:

$$u_1(X,z) = c\left[1 - \frac{h_1}{\eta_1} + \left(\frac{\eta_1^2}{6} - \frac{(h_1 - z)^2}{2}\right)\left(\frac{h_1\eta_1''}{\eta_1^2} - \frac{2h_1(\eta_1')^2}{\eta_1^3}\right)\right], \tag{25}$$

Lower layer fluid:

$$u_2(X,z) = c\left[1 - \frac{h_2}{\eta_2} + \left(\frac{\eta_2^2}{6} - \frac{(z + h_2)^2}{2}\right)\left(\frac{h_2\eta_2''}{\eta_2^2} - \frac{2h_2(\eta_2')^2}{\eta_2^3}\right)\right], \tag{26}$$

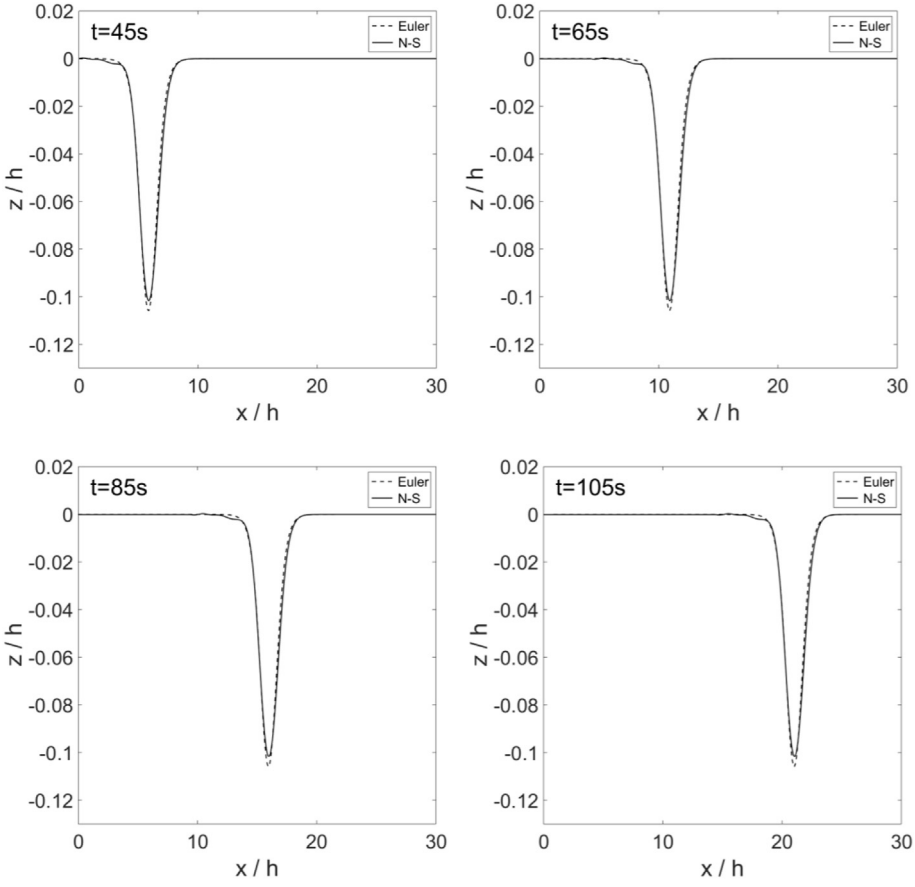

Fig. 10. The numerical results for the ISW waveforms with two different simulations for Case A2.

where $X = x - ct$, $\eta_1^{'} = \eta_{1X}$, $\eta_2^{'} = \eta_{2X}$, $\eta_1^{''} = \eta_{1XX}$, $\eta_2^{''} = \eta_{2XX}$, $\eta_1 = h_1 - \zeta$, and $\eta_2 = h_2 + \zeta$.

Except the region near the interface, the vertical distributions of horizontal velocities alter little in the upper and lower fluid. Overall, the results show that velocity distributions agree well with the theory.

It is worth mentioning that the proposed numerical model is based on the two-layer fluid approximation. Due to numerical diffusion, the density features a smooth transition near the interface in the beginning. Fig. 9 shows that the actual density profile at the trough of an ISW (t = 25s, 125s) for Case A2. Although the density distribution does not satisfy the two-layer fluid assumption, the deviation is not significant. Moreover, from 25s to 125s, the profile still remains the same. These facts suggest that the influence of numerical diffusion is limited though unavoidable.

In order to study the ISW loads, it is necessary to analyze the influence of fluid viscosity on the generation and propagation of ISWs, simulations based on the Navier-Stokes equations and the Euler equations are carried out. The wave profiles for Case A2 simulated by the two systems are shown in Fig. 10. We can see that the waveforms generated by the two simulation patterns remain stable and the amplitude does not decay obviously during the propagation of the ISW, with the relative error less than 5%. It is shown that the influence of fluid viscosity is limited.

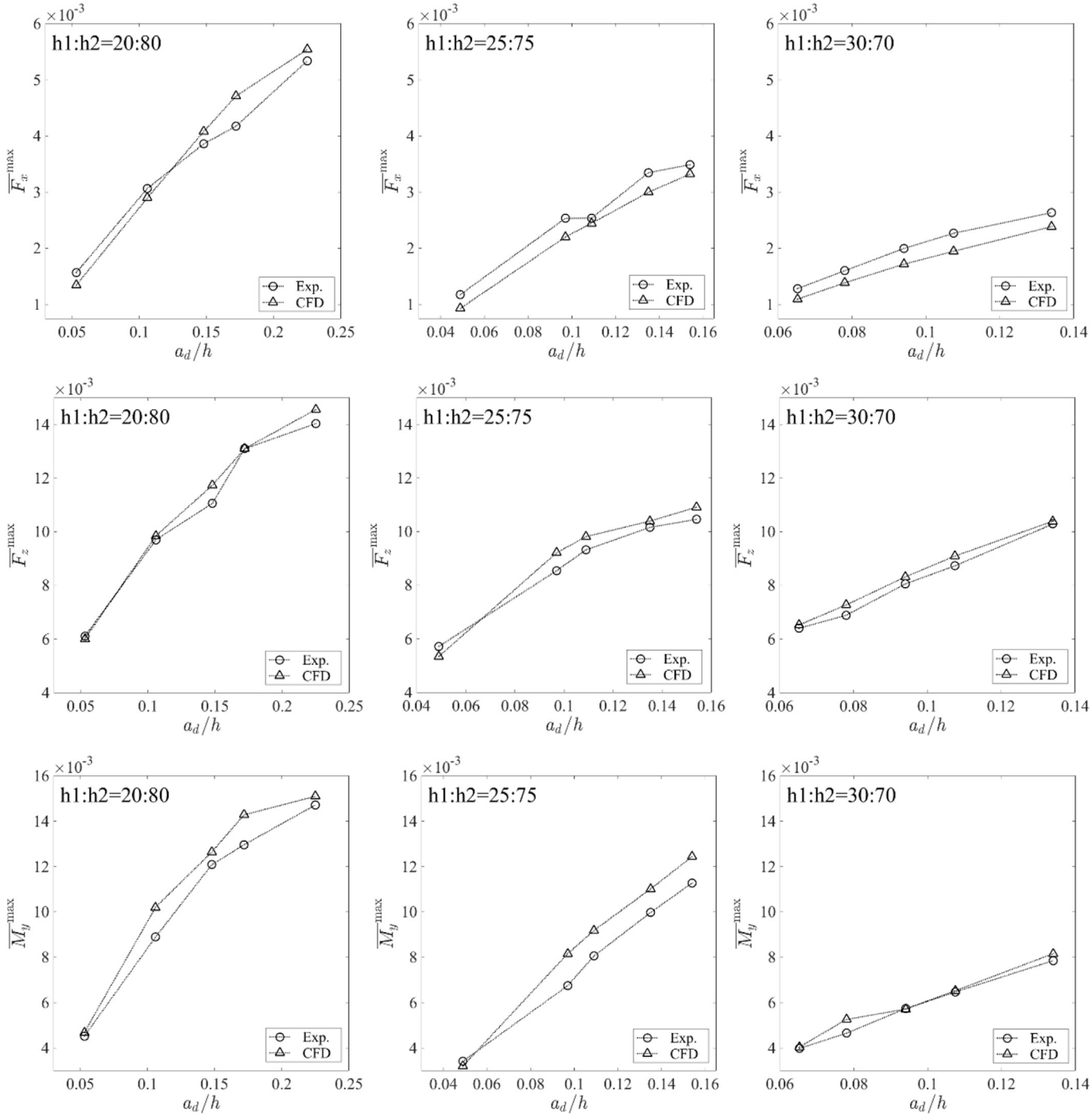

Fig. 11. Results of numerical and experimental amplitudes for dimensionless loads and torques.

4.3. Load characteristics on the semi-submersible platform

To facilitate discussion, we define $\overline{F}_x = F_x/(\rho_1 g\nabla)$, $\overline{F}_z = F_z/(\rho_1 g\nabla)$ and $\overline{M}_y = M_y/(\rho_1 gd\nabla)$ as the dimensionless horizontal vertical forces, and the torque respectively on the semi-submersible platform due to ISWs. The dimensionless loads and torques versus amplitudes are shown in Fig. 11, demonstrating that amplitudes for the horizontal and vertical forces, as well as the torque obtained numerically are in good agreement with the experimental results, with the maximum error less than 14%. The maximum error often shows up in the later stage (for example, Case B4 and Case B5) for each experimental setting. One possible reason is the deviation of the density structure from the strict two-layer configuration after several rounds of experiments.

Fig. 12 depicts the time variations of the dimensionless loads and torque for Case A2. The numerical and experimental results are in good agreement, which means that it is reasonable and feasible to calculate the loads and torque on the semi-submersible platform based on the proposed numerical flume. According to Eq. (15), the torque $\overline{M}_y$ is proportional to the horizontal load $\overline{F}_x$. Hence, we primarily focus on $\overline{F}_x$ and $\overline{F}_z$ in the subsequent analysis.

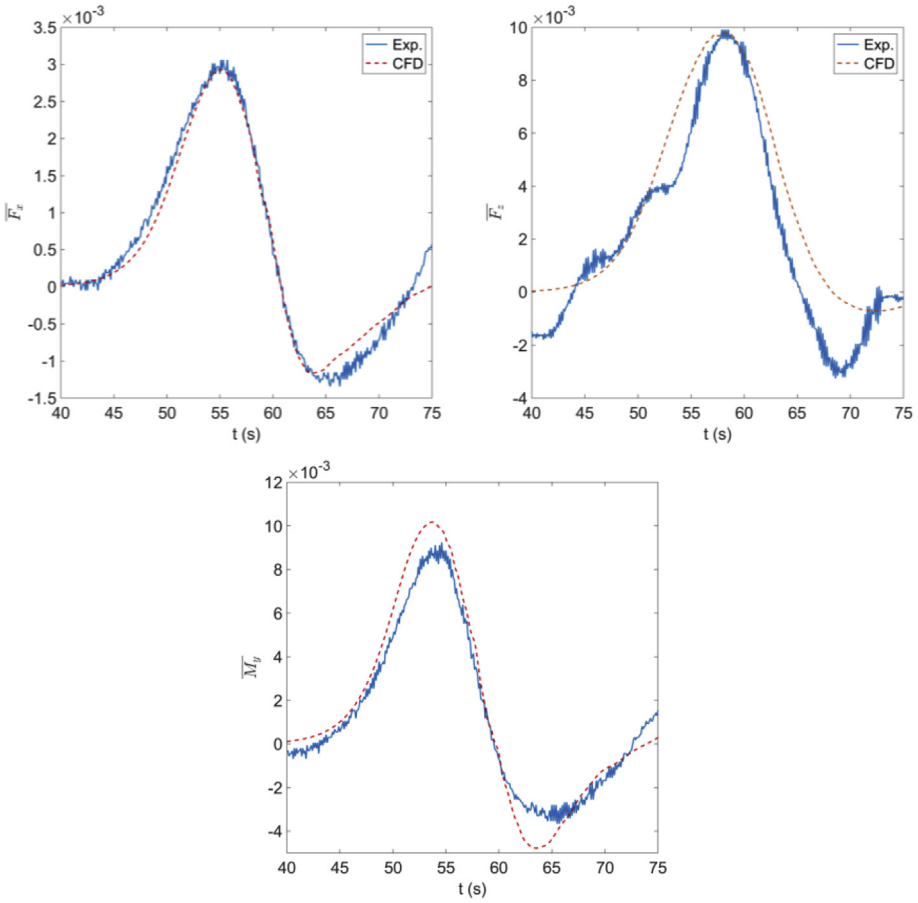

Fig. 12. The time variations of dimensionless loads and torque for Case A2.

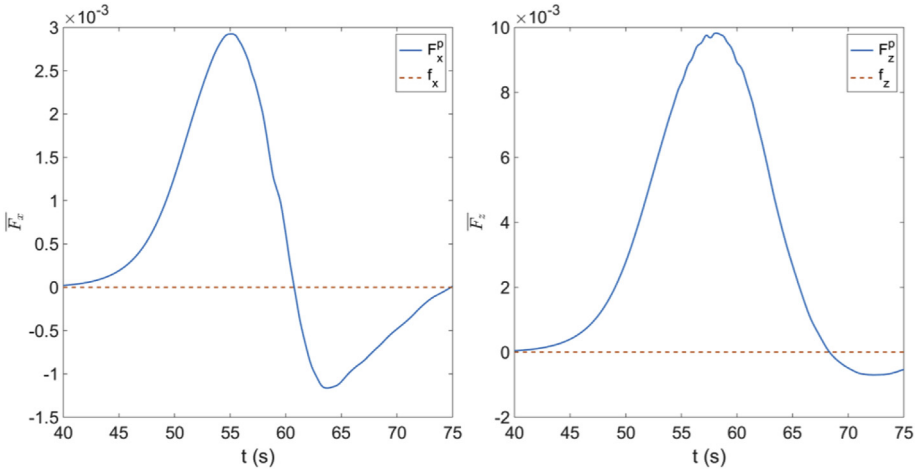

Fig. 13. The time variations of the pressure-difference and friction forces for Case A2.

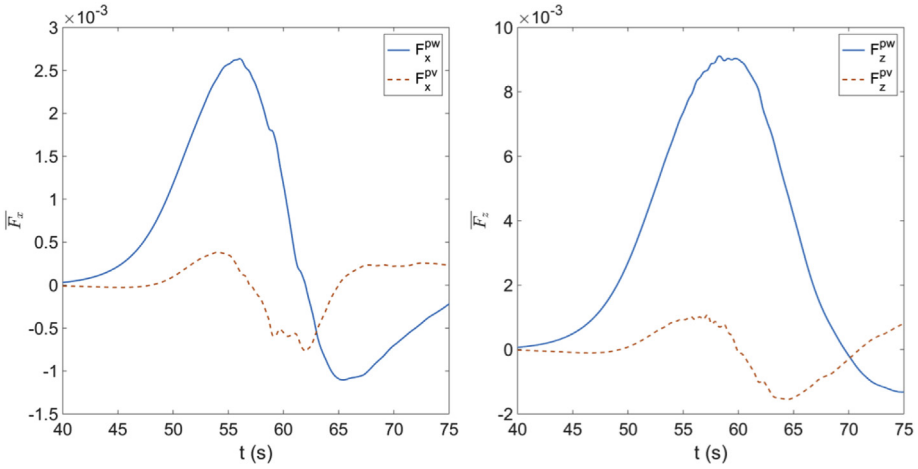

Fig. 14. The time variations of wave pressure-difference force (solid curve) and viscous pressure-difference force (dotted curves) for Case A2.

From Eqs. (13) and (14), it can be seen that the pressure-difference and frictions are two components of horizontal and vertical forces. The time variations of these two components for Case A2 are shown in Fig. 13. The results indicate that the pressure-difference force (F_x^p, F_z^p) is the dominant component, while the friction (f_x, f_z) is ignorable.

The time variations of wave and viscous pressure-difference forces due to ISWs for Case A2 are shown in Fig. 14. For the horizontal force, the viscous effect is significant (the absolute maximum of (F_x^p, F_x^{pv}) is (2.9e-3, 0.8e-3)), whereas for the vertical force, the viscous pressure-difference force is not important (the absolute maximum of (F_z^p, F_z^{pv}) is (9.8e-3, 1.3e-3)).

4.4. Numerical convergence

In order to verify the numerical convergence, simulations are performed with 3 different spatial resolutions of Case A2, and the measured maximum loads ($\overline{F}_x^{max}$, $\overline{F}_z^{max}$) and the relative errors of experimental results are listed in Table 2. The (N_x, N_y, N_z) represents the grid number in the x, y, z direction. Note that the grids are not uniformly distributed in the whole computation domain and the specific grid generation rule is already introduced in section 4.1.

Table 2
The numerical results for the grid-independence test (iteration step: 0.005s).

(N_x, N_y, N_z)	Grid quantity	$\overline{F}_x^{max}$(%)	$\overline{F}_z^{max}$(%)
(308,15,103)	1,901,898	2.86e-3 (6.79%)	9.91e-3 (2.15%)
(435,20,145)	3,403,996	2.90e-3 (5.49%)	9.85e-3 (1.53%)
(615,28,205)	7,531,188	2.90e-3 (5.49%)	9.84e-3 (1.42%)

Generally the more grid number, the smaller the numerical error. However, when the grid number is above a critical value, the error will not be significantly decreased but the computation cost increases. In Table 2, both the $\overline{F}_x^{max}$ and $\overline{F}_z^{max}$ are almost unchanged when grids are finer than the configuration (435, 20,145) employed in the present paper. It indicates that the numerical results with such grid distribution are stable and convergent.

4.5. The Froude-Krylov force and the diffraction effect

In this section, we discuss the interference of the platform in flow fields. For regular incident waves, the total non-viscous forces (F_x^{pw}, F_z^{pw}) acting on a floating structure include two parts: the Froude-Krylov force and diffraction force. The former is based on the Froude-Krylov assumption that the pressure distribution due to the incident wave is not affected by the presence of structure. The diffraction force is owing to the effect of the floating body which disturbs the waves.

Specifically, the Froude-Krylov forces (F_x^k, F_z^k) on a semi-submersible platform due to ISWs can be obtained by integrating the dynamic pressure P over the wetted surface S of the platform. Thus, the horizontal and vertical force components can be described as follows:

$$F_x^k = \int_S P n_x ds, \tag{27}$$

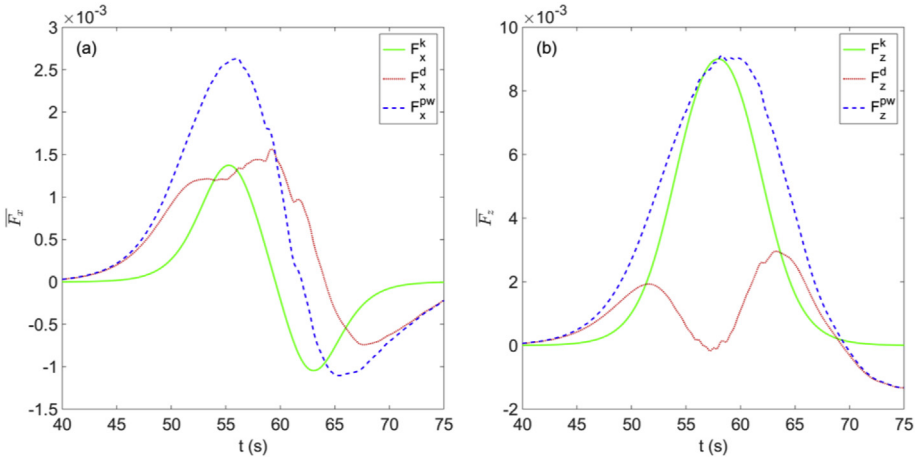

Fig. 15. The Froude-Krylov force and the diffraction force in the horizontal (a) and vertical (b) directions.

$$F_z^k = \int_S P n_z ds, \tag{28}$$

where P is determined by the Bernoulli equation. Taking the Froude-Krylov assumption (i.e. the pressure distribution due to the incident wave is not affected by the presence of the structure) into consideration, we have $v_i^2 = 0$. Hence, the dynamic pressure P induced by ISWs can be written as:

$$\mathrm{P} = -\rho_i\left(\frac{\partial \phi}{\partial t} + \frac{1}{2}\left(u_i^2 + w_i^2\right)\right), \tag{29}$$

where ϕ denotes the potential of the wave-induced velocity field, the horizontal velocities u_i are obtained by Eqs. (25) and (26), and the first-order approximation of vertical velocities w_i are given by:

$$w_i = (-1)^{i+1}\left(h_i + (-1)^i z\right)\overline{u}_{ix}, \quad with\ \overline{u}_{ix} = (-1)^i c\zeta \Big/ \left(h_i + (-1)^i \zeta\right). \tag{30}$$

Next, we can get the diffraction forces (F_x^d, F_z^d) by subtracting the Froude-Krylov forces (F_x^k, F_z^k) from the non-viscous forces (F_x^{pw}, F_z^{pw}).

The Froude-Krylov force F_x^k, the diffraction force F_x^d, and the non-viscous force F_x^{pw} are shown in Fig. 15(a). The F_x^k makes a considerable contribution to F_x^{pw}, which imply that the diffraction effect is not negligible.

In Fig. 15(b), it can be seen that the Froude-Krylov force F_z^k behaves very much similar to the non-viscous force F_z^{pw} as time evolves, and the diffraction force F_z^d is relatively limited. In addition to the conclusion drawn in Section 3.2 that the effect of fluid viscosity for the vertical force can be neglected, it is feasible to estimate the vertical ISW load by adopting the Froude-Krylov force.

5. Conclusions

Combined with laboratory experiments, a numerical flume based on the Navier-Stokes equations in a two-layer fluid is developed to simulate the nonlinear interactions between ISWs and a semi-submersible platform, where ISWs are generated by adding a mass source term and a sink term to the continuity equation in the source region located within the computational domain. The conclusions are summarized as follows:

(1) The waveform and amplitude of the ISW based on the developed numerical flume are in good agreement with the experimental and theoretical results. Moreover, numerical results for the horizontal and vertical forces, as well as torques on the semi-submersible platform due to the ISW are in good agreement with experimental results. Hence, it is feasible to simulate the nonlinear interactions between ISWs and semi-submersible platforms by the developed numerical flume.

(2) In general, hydrodynamic force of an offshore structure consists of three components: the wave and viscous pressure-difference components, and the friction component. However, for the case of a semi-submersible structure under the action of ISWs, the friction component is proved to be very small and can be neglected both for the horizontal and the vertical forces, and the viscous pressure-difference component is insignificant for vertical force. But the viscous pressure-difference component accounts for noticeable percentage of the horizontal force, implying significant effect of fluid viscosity. In addition, the vertical force of the structure exerted by an ISW can be estimated by means of the Froude-Krylov approach, which is of practical implication for engineering.

Acknowledgments

We acknowledge the financial support from the National Key R&D Program of China (2017YFC1404202), the National Natural Science Foundation of China (11602274, 11232012, 11572332 and 11372184), and the Strategic Priority Research Program of the Chinese Academy of Sciences (XDB22040203).

References

Ablowitz, M.J., Clarkson, P.A., 1991. Solitons, Nonlinear Evolution Equations and Inverse Scattering. Cambridge University Press.
Apel, J.R., Holbrook, J.R., Liu, A.K., Tsai, J.J., 1985. The sulu sea internal soliton experiment. J. Phys. Oceanogr. 15 (12), 1625–1651.
Bole, J.B., Ebbesmeyer, C.C., Romea, R.D., 1994. Soliton currents in the south China sea: measurements and theoretical modeling. In: Offshore Technology Conference, Houston, USA, pp. 304–307.
Cai, S.Q., Long, X.M., Gan, Z.J., 2003. A method to estimate the forces exerted by internal solitons on cylindrical piles. Ocean Eng 30 (5), 673–689.
Cai, S.Q., Long, X.M., Wang, S.G., 2008. Forces and torques exerted by internal solitons in shear flows on cylindrical piles. Appl. Ocean Res. 30 (1), 72–77.
Cai, S.Q., Wang, S.G., Long, X.M., 2006. A simple estimation of the force exerted by internal solitons on cylindrical piles. Ocean Eng 33 (7), 974–980.
Camassa, R., Choi, W., Michallet, H., Rusås, P.O., Sveen, J.K., 2006. On the realm of validity of strongly nonlinear asymptotic approximations for internal waves. J. Fluid Mech. 549 (549), 1–23.
Chen, M., Chen, K., You, Y.X., 2017. Experimental investigation of internal solitary wave forces on a semi-submersible. Ocean Eng 141 (9), 205–214.
Choi, W., Camassa, R., 2000. Weakly nonlinear internal waves in a two-fluid system. J. Fluid Mech. 313, 83–106.
Du, H., Wei, G., Gu, M.M., Wang, X.L., Xu, J.X., 2016. Experimental investigation of the load exerted by nonstationary internal solitary waves on a submerged slender body over a slope. Appl. Ocean Res. 59 (9), 216–223.
Faltinsen, O.M., 1993. Sea Loads on Ships and Offshore Structures. Cambridge University Press.
Helfrich, K.R., Melville, W.K., 2006. Long nonlinear internal waves. Annu. Rev. Fluid Mech. 38, 395–425.
Hirt, C.W., Nichols, B.D., 1981. Volume of fluid (VOF) method for the dynamics of free boundaries. J. Comput. Phys. 39 (1), 201–225.
Huang, W.H., You, Y.X., Shi, Q., Wang, J.Y., Hu, T.Q., 2013. The experiments of internal solitary wave loads and their theoretical model for a semi-submersible platform. Chin. J. Hydrodyn. 28 (6), 644–657 (in Chinese).
Koop, C.G., Butler, G., 1981. An investigation of internal solitary waves in a two-fluid system. J. Fluid Mech. 112, 225–251.
Kvittem, M.I., Bachynski, E.E., Moan, T., 2012. Effects of hydrodynamic modelling in fully coupled simulations of a semi-submersible wind turbine. Energy Procedia 24, 351–362.
Morison, J.R., Johnson, J.W., Schaaf, S.A., 1950. The force exerted by surface waves on piles. J. Petrol. Technol. 2 (5), 149–154.
Osborne, A.R., Burch, T.L., 1980. Internal solitons in the andaman sea. Science 208 (4443), 451–460.
Si, Z., Zhang, Y., Fan, Z., 2012. A numerical simulation of shear forces and torques exerted by large-amplitude internal solitary waves on a rigid pile in South China Sea. Appl. Ocean Res. 37 (8), 127–132.
Song, Z.J., Teng, B., Gou, Y., Lu, L., Shi, Z.M., Xiao, Y., Qu, Y., 2011. Comparisons of internal solitary wave and surface wave actions on marine structures and their responses. Appl. Ocean Res. 33 (2), 120–129.
Wang, X., Zhou, J.F., You, Y.X., 2017. A numerical wave-maker for internal solitary waves with timely updated mass source/sink terms. Eur. J. Mech. B Fluid 65, 274–283.
Wessels, F., Hutter, K., 1996. Interaction of internal waves with a topographic sill in a two-layered fluid. J. Phys. Oceanogr. 26 (1), 5–20.